Preprints (www.preprints.org) | NOT PEER-REVIEWED | Posted: 17 December 2018 doi:10.20944/preprints201812.0204.v1

Fluid Flow Turbulence in the Proximities of the Metal-Slag Interface in Ladle Stirring Operations

F.A. Calderón-Hurtado [1], R.D. Morales [2] and K. Chattopadhyay[3], S. García-Hernández [4]

[1] Graduate Student, IPN-ESIQIE, Department of Metallurgy, Ed. 7, Zacatenco, Mexico City 07738. Email: fabandrescal@gmail.com

[2] Professor, Instituto Politecnico Nacional-ESIQIE, Department of Metallurgy, Ed. 7, Zacatenco, Mexico City 07738, rmorales@ipn.mx, currently visiting Professor at the Department of Materials Science and Engineering, University of Toronto, 184 College Street, Suite 140, Toronto, Canada, M5S 3E4. Email: kinnor.chattopadhyay@utoronto.ca

[3] Dean's Catalyst Professor, Department of Materials Science and Engineering, Cross Appointed to Mechanical and Industrial Engineering, University of Toronto, 184 College Street, Suite 140, Toronto, Canada, M5S 3E4.

[4] Lecturer, Instituto Tecnológico de Morelia, Metallurgy Graduate Center, Av. Tecnológico No. 1500 C.P. 58120, Morelia, Michoacan, México, iq_sagahz@hotmail.com

Abstract

Three-phase interactions (metal-slag-argon) in ladle stirring operations have strong effects on metal-slag mass transfer processes. Specifically, the thickness of the slag controls the fluid turbulence to an extent that once trespassing a critical thickness, increases of stirring strength have not further effects on the flow. To analyze these conditions, a physical model considering the three phases was built to study liquid turbulence in the proximities of the metal-slag interface. A velocity probe placed close to the interface permitted the continuous monitoring and statistical analyses of turbulence. The slag-eye opening was found to be strongly dependent on the stirring conditions, and the mixing times decreased with thin slag thicknesses. Slag entrainment was enhanced with thick slag layers, and high flow rates of the gas phase. A multiphase model was developed to simulate these results finding a good agreement between experimental and numerical results.

Key Words: ladle stirring, turbulence, slag, interface, refining, mixing time, slag opening.

1. INTRODUCTION

Stirring of liquid steel in ladles through argon bubbling has various functions like thermal and chemical homogenization, speeding metal-slag mass transfer rates (melt desulfurization), supposedly floatation of inclusions and when necessary steel cool down to cast at the desired temperature. However, this operation is not unfortunately free from serious drawbacks. Among these we have the opening of a slag eye through which oxygen and nitrogen can be absorbed, possible slag entrainment if the stirring intensity of the bath is high, enhancement of melt-refractory and slag-refractory reactions which will degrade steel cleanliness. Another important operational factor, which depends on the steel tapping practice, oxygen and sulfur contents of steel at tapping and amount and type of additions, is the thickness of the slag layer. The thickness of this upper phase definitively influences the stirring conditions of the bath for a given energy input. It is a natural way of thinking that there must be a narrow operating window in the process to get the best from the contact among the various phases involved in this process. Thermally and chemically homogeneous baths, reasonable desulfurization rates lasting a span time from 5 to 8 minutes, low refractory wearing-rates and capture of inclusions that reach the metal-slag interface especially during the rising-time period are the goals of this process. For such a complex-multiphase system reaction-thermodynamics and fluid flow phenomena interact intimately in a way difficult to understand even nowadays. The present work is focused on fluid flow and specifically, on the turbulence of the liquid metal which is close to the metal-slag interface since this region is the critical one for floating inclusions.

Fluid flow of liquid steel in ladles has been studied from many points of view using physical and mathematical models. The structure of the gas-liquid plume was studied using a mechanistic approach by Krishnapisharhody and Irons [1,2] establishing models to estimate the size of the slag eye opening area (SEO) and the height of the spout region as function of bath height and gas flow rate. The same authors developed correlations linking averaged velocities of the liquid and gas phases and gas volume fraction along the plume height as functions of gas flow rate and bath height [3]. Spout height was defined through a dimensionless variable involving gas flow rate [4] presenting a unified theory for two-phase flows dynamics in the plume [5]. Mixing times are considered as a useful information to estimate the thermal and chemical homogenization speediness of steel in ladles under some given flow rate of gas. Various authors have proposed simple engineering correlations to estimate the mixing time for gas-liquid systems [6]. On this line Mazumdar and Guthrie [7-9] estimate this parameter and the plume velocity

© 2018 by the author(s). Distributed under a Creative Commons CC BY license.

Preprints (www.preprints.org) | NOT PEER-REVIEWED | Posted: 17 December 2018 doi:10.20944/preprints201812.0204.v1

(it is the averaged two-phase velocity in the plume) through the ladle dimensions and the flow rate of the bubbling gas. **Table 1** shows these correlations for two-phase, gas-liquid flows according to other researches [6-11]. However, in actual steel ladle systems the influence of the layer on the mixing time indicates the mixing times are larger than for two-phase flows [12-14]. All these studies report that the thickness of the slag weakens the mixing kinetics in steel; even it can be said that the thickness of the slag is more important than its physical properties in this regard [15, 16]. It must be said that low viscosity slags enhance mass transfer between both phases, tough slag entrainment in the melt can be brought on by rises of gas flow rate [17]. The correlations so far reported up to date, to calculate mixing times with an upper slag are presented in **Table 2** [10-11]**, [**16], [18-21]**.** Steel eye opening (SEO) area is another important parameter of the process since, depending on its size, steel can be less or more contaminated by the atmospheric air. Its measurement, through infrared video-cameras, is also important to know the actual flow rates of argon as the injection through the porous plug is, most of the times, inaccurate due to the partial obstruction of the plug surface by debris of metal and slag or leaks. One of the first works attempting to study the process conditions on the SEO area was that of Yonezawa and Schwertdfeger [22] and Subagyo et. al. [23] The operating process parameters factors affecting the size of the SEO are summarized in **Table 3** [24, 25].

Table 1. Mixing time correlations for baths without an upper layer.

Reference	Mixing Time	Energy	Units of energy
1. Haida et al. [10]	$\tau_m = 100\dot{\varepsilon}^{-0.42}$ (1)	$\dot{\varepsilon} = \frac{\rho_L g Q H_L}{\rho_L \pi R^2 H_L}$	W/ton
2. Ying et al. [11]	$\tau_m = 125\dot{\varepsilon}^{-0.289}$ (2)	$\dot{\varepsilon} = \frac{\rho_L g Q H_L}{\rho_L \pi R^2 H_L}$	W/ton
3. Mazumdar and Guthrie. [7-9]	$\tau_m = 37\varepsilon_m^{-0.33} H_L^{-1} R^{1.66}$ (3)	$\dot{\varepsilon} = \frac{\rho_L g Q H_L}{\rho_L \pi R^2 H_L}$	W/kg
4. Iguchi et al. [6]	$\tau_m = 1200 Q_g^{-0.47} D^{1.97} H_L^{-1} v_L^{0.47}$ (4)		

ρ_L liquid density, g is gravity constant, Q is gas flow rate, H_L is bath height, R ladle radius, D is ladle diameter, v_L kinematic viscosity of the liquid.

2. EXPERIMENTAL SETUP

The experimental setup consists of a 1/3 scale ladle, made of transparent plastic, of a billet company located in Mexico equipped with a bottom plug to stir steel with argon. The dimensions of the model and the positions of the plug and the slide gate are reported in **Figures 1a and 1b**. The ladle is filled with tap water through a top pipe until the operational scaled-height corresponding to the plant. Injection of argon is modeled using air instead, which is supplied by an air compressor and injected through an orifice in the ladle bottom, with a pressure of 2.5 kg/cm^2. The gas flow rate is measured through a mass flowmeter located between the compressor and the injection point. The lighter phase is food-oil and a layer of this material is conformed before starting the experiment to obtain a desired thickness. To have visualization records of the experiments, two video cameras were placed, one on the top of the bath and another one facing the wall of a flat chamber attached outside the ladle wall filled with water to avoid optical distortions from the curvature of the vessel. The camera in the top recorded the images of the bath surface without and with an oil layer. The video recordings were decomposed into images of the eye opening with a frequency of 2 s^{-1}. Quantitative measurements of these areas were performed using a previously calibrated image analyzer software [26], following a similar procedure as that reported by Peranandhathan and Mazumdar [25].

Preprints (www.preprints.org) | NOT PEER-REVIEWED | Posted: 17 December 2018 doi:10.20944/preprints201812.0204.v1

Table 2. Mixing time correlations for a denser phase with a lighter top layer. 16)

Reference	Correlation	N	r/R	Θ	Top Layer
1. Haida et al. [10]	$\tau_m = 100\dot{\varepsilon}^{-0.42}$	1	0, 0.5		Polystyrene balls
2. Ying et al. [11]	$\tau_m = 125\dot{\varepsilon}^{-0.289}$	1	0		
3. Yamashita el al. [18]	$\tau_m = 1910 Q_g^{-0.17} D^{1.49} HL^{-1.0} V_L^{0.47} \left[\frac{PL-Ps}{PL}\right]^{0.243}$	1	0		Silicon oil and pentane
4. Mazumdar-Kumar [19]	$\tau_m = 60.2 Q_g^{-0.33} R^2 H_L^{-1.0} h_s^{0.6} \left[\frac{\sigma_s}{\mu_s}\right]^{-0.022}$	2	0.5	180	Petroleum ether, mustard oil and benzene
5. Patil et al. [20]	$\tau_m = 152 Q_g^{-0.33} R^{2.33} H_L^{-1.0} \left(\frac{h_s}{H_s}\right)^{0.3} V_s^{0.033} \left[\frac{P_L - P_S}{P_L}\right]^{-0.044}$	1 2	0.5 0	180	Petroleum ether, mustard oil and benzene and silicon oil
6. Khajavi-Barati et al [16]	$\tau_m = 2.33 \dot{\varepsilon}_{ms}^{-0.34} H_{eff}^{-1.0}$	1	0		Kerosene and silicon oil
7. Amoro et al. [21]	$\tau_m = 9.83 N^{-0.1025} \dot{\varepsilon}^{-0.364} \left(\frac{r}{R}\right)^{-0.0051} \left[\frac{h_s}{H_L}\right]^{0.044}$	1,2 3	0.33 0.5 0.67 0.80	120 180	Engine oil blue, engine oil red and soybean oil

τ_m represents mixing time (s), Q is gas flow rate, D and H are diameter and height of the container respectively, ν_s is the kinematic viscosity of the lighter phase, ν_L is the kinematic viscosity of the denser phase, ρ_L and ρ_s represent the densities of the denser and lighter phase respectively, μ_s is the dynamic viscosity of the lighter phase, σ_s is the surface tension of the lighter phase, $\dot{\varepsilon}$ is the specific potential energy input in W/ton, except for Khajavi and Barati [15] in W/kg, h_s is the thickness of the lighter phase, N is the number of nozzles, θ their separation angle and H_{eff} is and effective height including the denser and lighter phases as defined by Khajavi and Barati [15]. The units of all other variables are expressed in SI units. This table was complemented with the last row in the present work.

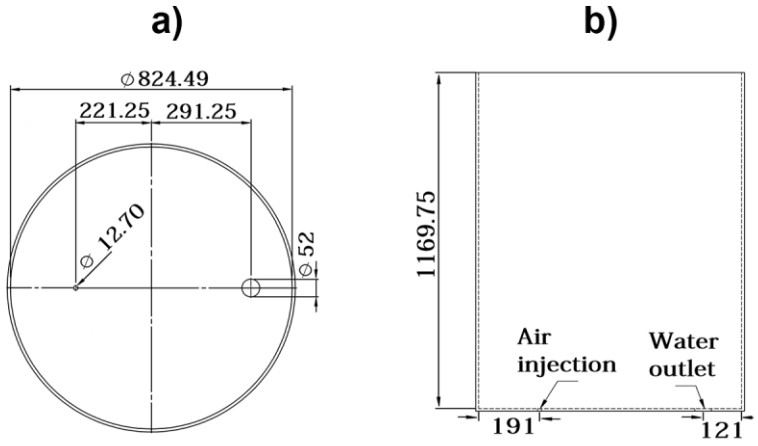

Figure 1. (a) Dimensions of the model (mm). (b) Position of the nozzle.

Preprints (www.preprints.org) | NOT PEER-REVIEWED | Posted: 17 December 2018 doi:10.20944/preprints201812.0204.v1

Table 3. Correlations to estimate the size of the open steel eye during stirring operations in ladles.

Ref.	Correlation	N	r/R	Systems	Constraints
[22]	$log\left(\frac{A_{es}}{h_s H}\right) = -0.69879 + 0.90032\, log\left(\frac{Q^2}{g h_s^5}\right) - 0.14578\left[log\left(\frac{Q^2}{g h_s^5}\right)\right]^2 + 0.0156\left[log\left(\frac{Q^2}{g h_s^5}\right)\right]^3$ **(1)**	1	0	Mercury-oil Liquid steel-slag	$\Phi_{orifice}$=0.5 mm $0.01 \le \frac{Q^2}{g h_s^5} \le 10000$ Other diameters of the orifice give different correlations
[23]	$\frac{A_{es}}{(h_s + H)^2} = 0.02 \mp 0.002\left(\frac{Q^2}{g h_s^5}\right)^{0.375 \mp 0.0136}$ **(2)**		0, 1	Mercury-oil Liquid steel-slag	It is a modification of the precedent correlation
[24]	$\frac{A_e^*}{A_p^*} = -0.76(Q^*)^{0.4} + 7.15(1-\rho^*)^{-1/2}(Q^*)^{0.73}(h^*)^{-1/2}$ $Q^* = \frac{Q}{g^{0.5} H^{2.5}}$, $A_e^* = \frac{A_e}{H^2}$, $A_p^* = \frac{A_p}{H^2} = 1.41(Q^*)^{0.4}$, $\rho^* = \frac{\rho_s}{\rho_L}$, **(3)** $h^* = \frac{h_s}{H}$	1	various	Water-paraffin, water-motor oil, $CaCl_2$-paraffin oil, Hg-silicon oil, water-silicon oil and steel-slag	Assumed to be for general application of various systems and different orifice positions
[25]	$\frac{A_e}{h_s H} = 3.25\left(\frac{U_p^2}{g h_s}\right)^{1.28}\left(\frac{\rho_L}{\Delta\rho}\right)^{0.55}\left(\frac{\nu_s}{h_s U_p}\right)^{-0.05}$ $U_p = 17.4 Q^{0.244} H^{-0.08}\left(\frac{\rho_g}{\rho_L}\right)^{0.0218}$ **(4)**	1	0, 0.5	Water-petroleum-ether, water-coconut oil, water-mustard oil	Applicable for $\varepsilon \sim 0.01$ W/kg, $0.75 < H/D < 1.5$, $\nu \sim 10^{-6}\frac{m^2}{s}$, and $0.006 < h_s < 0.05$ For centric position of the orifice

All correlations are given in SI units. Q is gas flow rate, h_s is slag thickness, H is the height of the denser phase, U_p is plume velocity, A_p is the plume area, A_e is the area of the eye opening, ν_s is kinematic viscosity of the lighter phase, ρ_s and ρ_L are densities of the lighter and denser phases respectively. The plume velocity was calculated using the equation of Yonezawa and Schwerdtfeger [22].

Preprints (www.preprints.org) | NOT PEER-REVIEWED | Posted: 17 December 2018 doi:10.20944/preprints201812.0204.v1

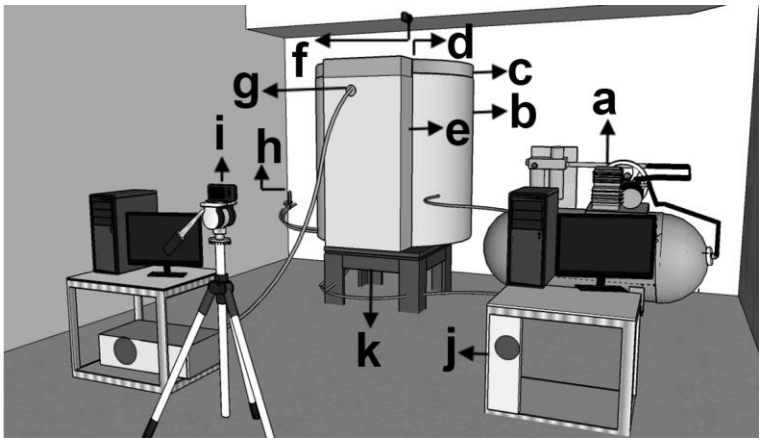

Figure 2. Experimental set up. a) Air compressor. b) Water. c) Oil layer. (d) Tracer injection. e) Flat chamber. f) Upper camera. g) Ultrasonic transducer. h) Mass flowmeter. i) Frontal camera. j) Colorimeter cell. k) Air injection.

Twenty cubic centimeters of an aqueous solution of food red-colorant was employed as tracer, injected 100 mm below the bath surface near the geometric center of the ladle. A peristaltic pump was used for extracting samples from the bath which were fed into a colorimeter cell to obtain the instantaneous concentration of the tracer. The analogical signals of the colorimeter are converted into digitals ones through a data acquisition card in a PC permitting real-time plotting of the tracer concentration vs time. Fluid flow turbulence was captured through a 10 million Hertz ultrasonic transducer or probe immersed in the bath 20 mm below its surface and located in the ladle wall just opposite to the wall which is nearest to the injection orifice. This probe measured the horizontal velocities in the bath at this plane as well as all turbulent variables associated with the flow. **Figure 2** shows a scheme of the experimental setup, here described. The physical properties of the three phases, water, oil and air as well as other details of the experimentation are shown in **Table 4**.

Table 4. Experimental conditions and physical properties of the multiphase model.

Flow rates of gas	m^3/s Model	$5.33X10^{-5}$	$1.07X10^{-4}$	$2.14\ X10^{-4}$	$4.28X10^{-4}$	$5.50X10^{-4}$
	l/min Ladle	52	100	200	400	500

Physical properties of fluids (293 K)				
	Density	**Viscosity**	**Surface tension**	**Interfacial tension**
Water	1000	0.001003	0.073	0.0565
Oil	913	0.060	0.040	
Air	1.24	$1.8X10^{-5}$		
Other features: Nozzle diameter is 6 mm, bath height is 0.90 m, scale up criterion is the Fr number.				

3. THE MULTIPHASE MODEL

To simulate the interaction among the multiphase system, the Volume of Fluid Model (VOF) was applied [27]. This model uses a common pressure-velocity field by solving a single set of momentum transfer equations and uses as a phase indicator,

Preprints (www.preprints.org) | NOT PEER-REVIEWED | Posted: 17 December 2018 doi:10.20944/preprints201812.0204.v1

for including the presence of interfaces, the volume fraction of a phase by the solving the corresponding advection equation. The equation of the phase indicator is,

$$\frac{\partial \alpha_i}{\partial t} + (u_m \cdot \nabla)\alpha_i = 0 \qquad (1)$$

unit value of α_i corresponds to a cell full of fluid 1, while a zero value indicates that the cell contains no fluid 1. To avoid numerical diffusion the equation should be solved using second order explicit discretization equation in time and space, updating the indicator through the velocity field] [28]. The pressure-velocity field is simulated by resolving the continuity and Navier-Stokes equations,

$$\nabla \cdot u_k = 0 \qquad (2)$$

$$\frac{\partial v_k}{\partial t} + u_k \cdot \nabla u_k = -\frac{1}{\rho_k}\nabla p_k + \nu_k \nabla^2 u_k \qquad (3)$$

Where the u_k is the Reynolds Averaged Navier-Stokes (RANS) velocity of the turbulent flow. The interface boundary conditions or momentum jump conditions are expressed as,

$$\sum_{k=1}^{2} T_k n_k = 2\sigma_I H_I n_I \qquad (4)$$

Where $\sigma_I, H_I \; and \; n_I$ are the surface tension, the radius of curvature and the normal vector to the interface which was simulated through the Continuous Surface Model of Brackbill [29]. For the present case the physical properties of the multiphase system, (including the food oil [35]), are calculated as,

$$\rho_m = \rho_w \alpha_w + \rho_o \alpha_o + \rho_a \alpha_a \qquad (5)$$

$$\mu_m = \mu_w \alpha_w + \mu_o \alpha_o + \mu_a \alpha_a \qquad (6)$$

The constraint for the volume fraction is,

$$\alpha_w + \alpha_o + \alpha_a = 1 \qquad (7)$$

Where the sub-indexes **w**, **o** and **a** hold for water, oil and air, respectively. The k-ε model [30, 31] was used to simulate the turbulence of the flow combined with equations (2) and (3) to obtain the pressure-velocity field which is employed to update the advection equation of the indicator. The model, which is based in the turbulent viscosity hypothesis [31], requires the solution of two other equations for the turbulent kinetic energy and its dissipation rate,

$$\frac{\partial(\rho_m k)}{\partial t} + \frac{\partial(\rho_m k u_i)}{\partial x_i} = \frac{\partial}{\partial x_j}\left[\left(\mu_m + \frac{\mu_m^t}{\sigma_k}\right)\frac{\partial k}{\partial x_j}\right] + C_{1\varepsilon}\frac{\varepsilon}{k} + G_k + G_b - \rho_m \varepsilon \qquad (8)$$

$$\frac{\partial(\rho_m \varepsilon)}{\partial t} + \frac{\partial(\rho_m \varepsilon)}{\partial x_j} = \frac{\partial}{\partial x_j}\left[\left(\mu_m + \frac{\mu_m^t}{\sigma_\varepsilon}\right)\frac{\partial}{\partial x_j}\right] + C_{1\varepsilon}\frac{\varepsilon}{k}(G_k + C_3\varepsilon G_b) - C_{2\varepsilon}\rho_m \frac{\varepsilon^2}{k} \qquad (9)$$

G_k is the generation of kinetic energy due to the interaction between the gradients of the mean velocity and the Reynolds stresses (energy extracted from the mean flow):

$$G_k = -\rho_m u_i' u_j' \frac{\partial u_k}{\partial x_j} \qquad (10)$$

And G_b is the energy generated by buoyancy forces and is given by equation (11):

$$G_b = -g_i \frac{\mu_m^t}{Pr_t}\frac{\partial \rho_m}{\partial x_i} \qquad (11)$$

The scalars k and ε are used to calculate the turbulent viscosity through equation (12),

$$\mu_m^t = \rho_m C_\mu \frac{k^2}{\varepsilon} \qquad (12)$$

Where C_μ=0.09, $C_{1\varepsilon}$=1.44, $C_{2\varepsilon}$=1.92, σ_k=1.0, σ_ε=1.3, $C_{3\varepsilon}$=1.0.

The solution of the governing equations with boundary conditions & all source terms are obtained through the commercial package ANSYS [32]. In all solid surfaces a no-slip boundary condition is applied, and the wall log-law is used to link the outer grid with the computational elements in the boundary layer. In the nozzle, an entry gas-velocity boundary condition was applied and in the top surface of the bath a pressure one was applied. The calculation domain was divided by polyhedral cells and the calculation were conducted under transient conditions. A criterion for convergence was fixed when all residuals for the dependent variables add up to less than 10^{-4}.

Preprints (www.preprints.org) | NOT PEER-REVIEWED | Posted: 17 December 2018 doi:10.20944/preprints201812.0204.v1

4. RESULTS AND DISCUSSION

4.1 Flow parameters

The mixing times, for the two-phase flow, were calculated using the experimental conditions of **Table 4** and the correlations in **Table 1**. These calculated mixing times are compared with the corresponding experimental mixing times and the two values are plotted in **Figure 3a**. Here it is evident that the correlations 1 and 3 are the most approximated to the experimental measurements. Since the presence of the upper phase affects the fluid dynamics of the lower phase the same procedure is applied for calculating the mixing times of the three-phase system (two immiscible liquids and gas phase) using the correlations of Table 2 and comparing these values with the experimental measurements. The results are presented in **Figure 3b**, where, as it is evident, 5 predicts values which are very approximated to the experimental ones. Observing carefully these two correlations for the two-phase and three-phase flows and given their highest accuracy in predicting the experimental mixing times the following observations can be established:

1. For two-phase flows, mixing time is basically dependent on the stirring energy, the bath height and on the geometry of the ladle.
2. Tall baths favor smaller values of the mixing time.
3. For three-phase flows, thicker slags increase the mixing time.
4. The mixing time is basically independent from the physical properties of the upper phase such as density and viscosity and depends more on its thickness.

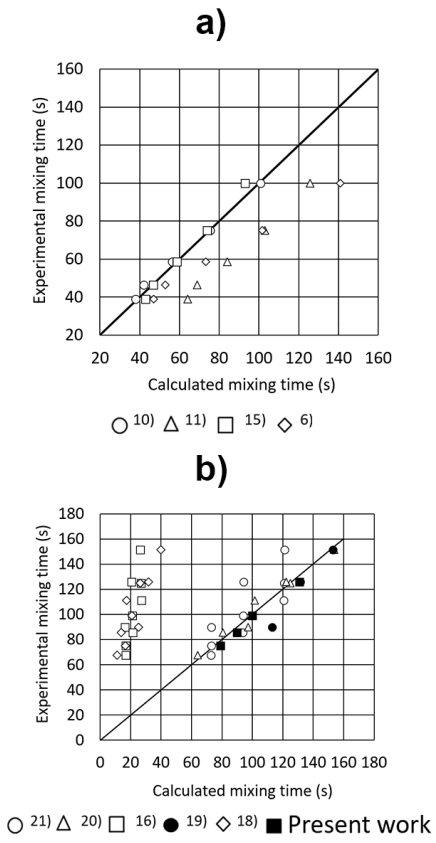

Figure 3. Experimental vs calculated mixing times. a) Bath without an upper layer. b) Bath with an upper layer.

The later observation is the most oriented to discussion as someone would intuitively think that the physical properties of the slag or upper phase would be determinant. However, it is evident from the presented results and those of other researchers that the control of mixing is essentially the thickness due to the dissipation rate of kinetic energy when the gas-liquid plume strains

Preprints (www.preprints.org) | NOT PEER-REVIEWED | Posted: 17 December 2018 doi:10.20944/preprints201812.0204.v1

the interface. That is, once the liquid, driven by the buoyancy forces imparted by the bubbles, reaches the interface, the upper phase is displaced receding toward the ladle wall forming the spout where the bubbles burst consuming energy in the process.

The experimental SEO areas along the experimental time are shown in **Figure 4,** these areas suffer natural variations due to the turbulence of the flow but tend to reach constant values for any given operating condition.

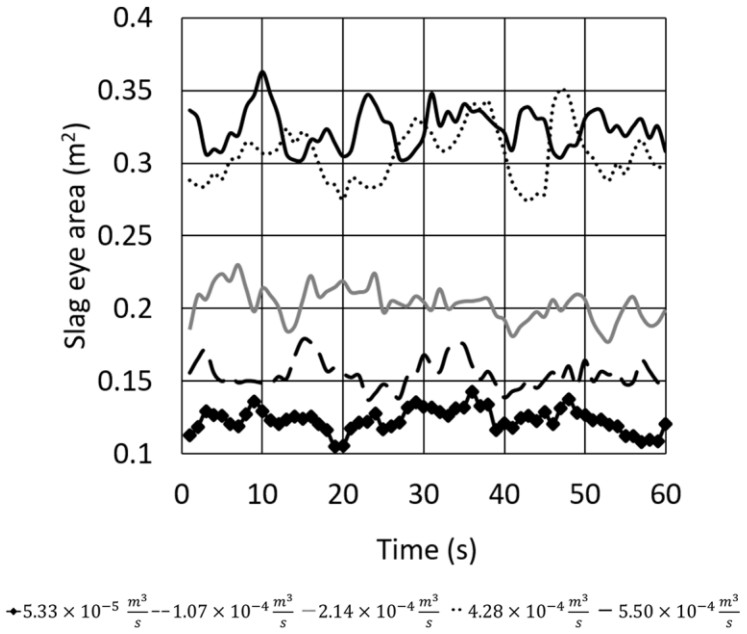

Figure 4. Effects of gas flow rate for an upper layer thickness of 0.02 m on the variations of the eye-opening area with time.

Figure 5 shows the SEO areas simulated with the mathematical model and compared with corresponding photos of the experimental SEO areas. As seen, there is a very good qualitative agreement between the mathematical simulations and the experimental SEO areas, even, the shapes of the SEO's are very similar.

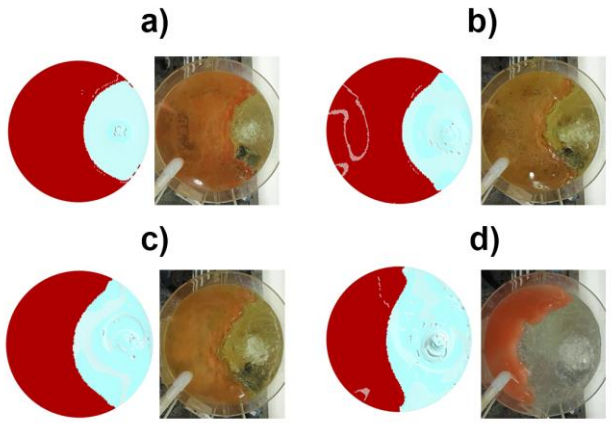

Figure 5. Comparison between experimental and numerical views of the slag eye opening area for an oil thickness 0.02 m. (a) flow 5.33 x 10^{-5} m^3/s. (b) 1.07 x 10^{-4} m^3/s. (c) 2.14 x 10^{-4} m^3/s. (d) 4.28 x 10^{-4} m^3/s.

To test the quantitative capacity of the mathematical model to predict the experimental SEO areas, the images of the digital images and the areas of the corresponding photos in **Figure 5** were measured with the image analyzer. The results of the digital

Preprints (www.preprints.org) | NOT PEER-REVIEWED | Posted: 17 December 2018 doi:10.20944/preprints201812.0204.v1

or numerical SEO areas are compared with the measured SEO areas in **Figure 6** and as is seen the agreement is excellent, granting the reliability of the mathematical model to study the dynamics of the three-phase flow system. In the same Figure, the SEO areas calculated with the correlations of Table 3, can be compared with the experimental SEO's and it is evident that the best correlation is the number 4. Therefore, this correlation is recommended as simple engineering tool to estimate the SEO for operating steel ladles. Accordingly, it can be said that the present mathematical model is useful to test he reliability of engineering correlations for calculating the mixing time and the SEO areas.

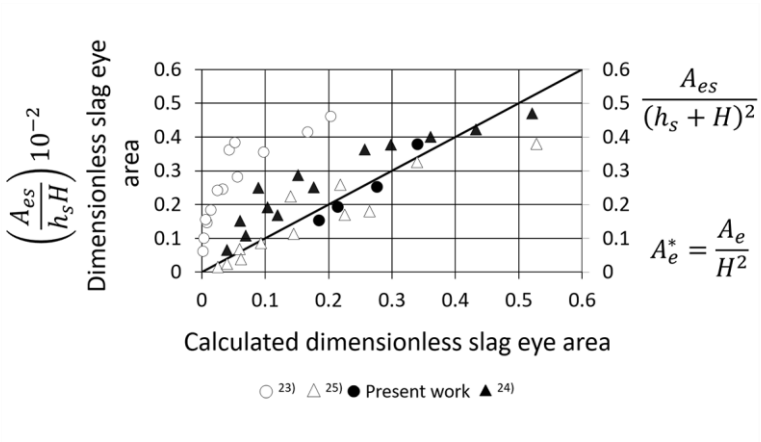

Figure 6. Slag eye opening area.

4.2 Flow Structure

The presence of a slag or an upper layer decreases the turbulence of the denser liquid as is seen in **Figures 7a-7b** for the velocity field in a vertical plane passing through the axis of the injector without and with a 0.01 m thick layer, respectively. Without an upper layer, the recirculating flow is large enough to include the full plane. However, even a thin upper layer restricts the recirculating flow forming a free shear boundary layer in the upper right extreme, near the ladle wall. **Figures 7c-7d**, show the velocity fields in perpendicular planes to those shown in **Figures 7a and 7b**.

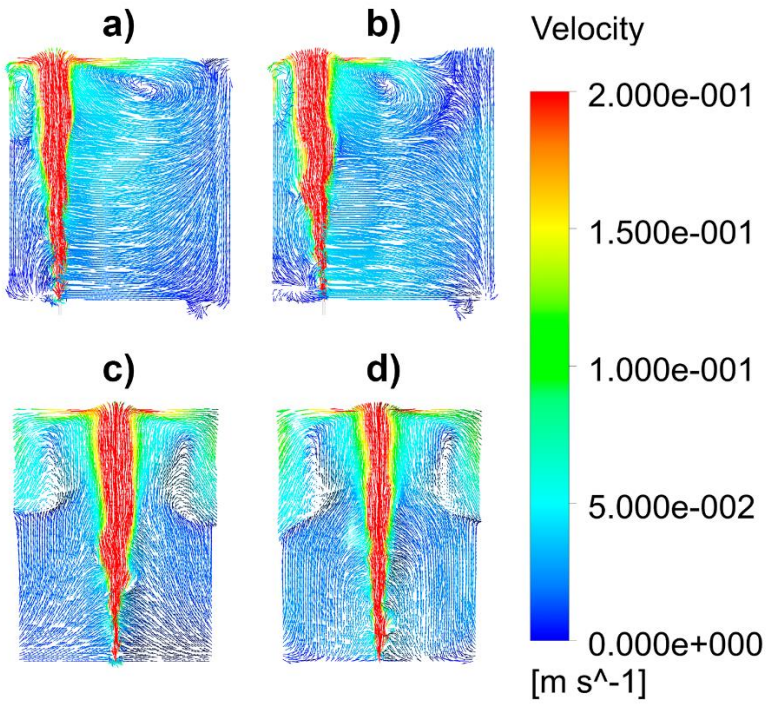

Figure 7. Simulated velocity fields of the liquid phase for a gas flow rate of $2.14 \times 10^{-4}\ \frac{m^3}{s}$ and different thicknesses of the oil layer. Front view a) 0 m. b) 0.01 m. Side view c) 0 m. d) 0.01 m.

Preprints (www.preprints.org) | NOT PEER-REVIEWED | Posted: 17 December 2018 doi:10.20944/preprints201812.0204.v1

As seen, in these planes more than half of these planes have small fluid velocities and last third of the upper region is subjected to the effects of recirculating flows induced by the two-phase plume. **Figures 8a and 8b** correspond to Figures 7a and 7b with upper layer thicknesses of 0.02 and 0.04 m, respectively. The thicker upper layers constrain more the upper recirculating flow leaving larger regions of small liquid velocities. Once the plume reaches the bath surface encounters the upper layer which offers resistance by receding forming the spout. **Figures 8c and 8d**, show the velocity fields in planes which are perpendicular to those shown in **Figures 8a and 8b,** respectively. The regions with small velocities increase considerably, with an upper layer of 0.02 m there is still a recirculating flow in the denser flow that takes contact with the upper phase. However, when the upper layer thickness is 0.04 the contact between the denser and upper layer is constrained to a very limited area surrounding the spout. Under these conditions the exchange between both liquid phases is very poor and from a practical point of view very small refining capacity is left and the capture of inclusions is limited. Since we use a 1/3 scale model that means that a thick 0.12 m slag would keep stagnant practically all the melt for a flow a rate of 100 l/min. An option is to increase the flow rate of argon to intensify the contact between both liquids, but thick slags are easily entrained in the melt bulk [33] increasing the presence of inclusions.

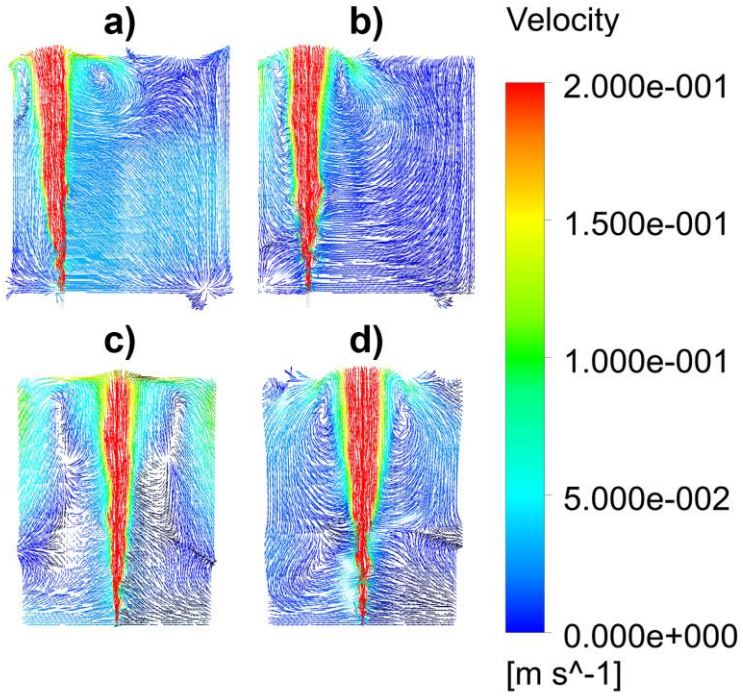

Figure 8. Simulated velocity fields of the liquid phase for a gas flow rate of $2.14 \times 10^{-4}\ \frac{m^3}{s}$ and different thicknesses of the oil layer. Front view a) 0.02 m. b) 0.04 m. Side view c) 0.02 m. d) 0.04 m.

Figures 9a and 9b show the velocity fields in horizontal planes at different bath heights, for a ladle without and with an upper layer 0.01 m thick. Without the upper layer horizontal-rotating motions are observed, but even the presence of a thin upper layer changes the flow pattern to divided recirculating flows ate each side of the plume. Thicker layers of 0.02 and 0.04 m in **Figures 10a and 10b** respectively intensify the split of the velocity fields at each side of the plume, though, with a 0.02 m thick layer the motion in the liquid bulk is still appreciable. Hence, a layer of 0.06 m in the actual ladle is thin enough to maintain good stirring conditions and even increase the flow of rate of gas to intensify the mass transfer during the desulfurization process. This thickness represents 2.2 % of the total bath height and it is recommendable since it keeps a volume large enough to capture inclusions and to desulfurize steel. Thinner layers will not be enough to keep dissolved all the sulfur necessary for a given steel grade and thicker slags will constrain the motion of steel decreasing its contact with the slag.

Preprints (www.preprints.org) | NOT PEER-REVIEWED | Posted: 17 December 2018 doi:10.20944/preprints201812.0204.v1

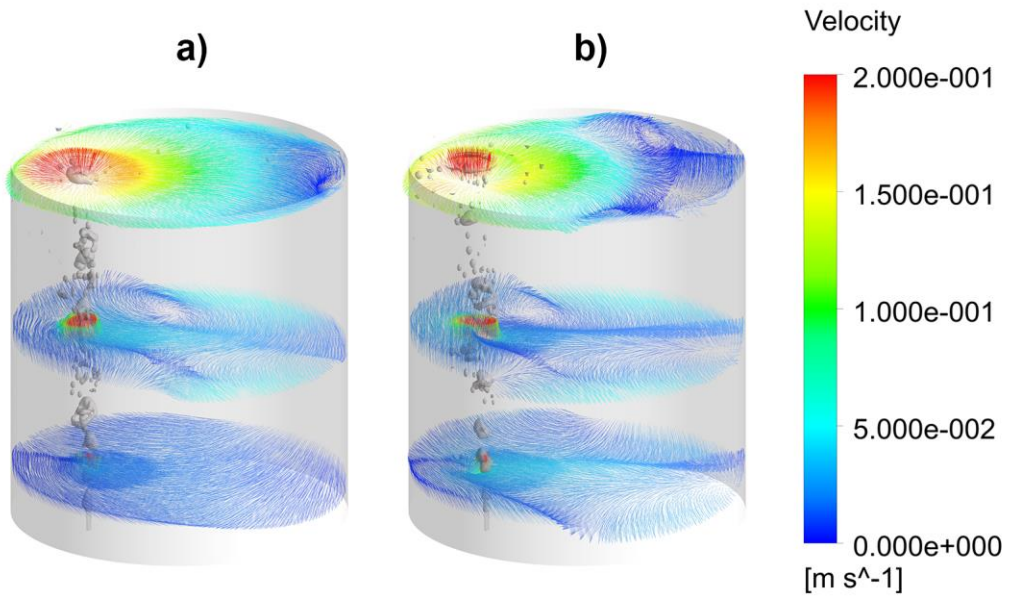

Figure 9. Simulated velocity fields of the liquid phase in different horizontal planes, at 100 mm, 450 mm and 880 mm, for a gas flow rate of $2.14 \times 10^{-4}\ \frac{m^3}{s}$ and different thicknesses of the oil layer. a) 0 m. b) 0.01 m.

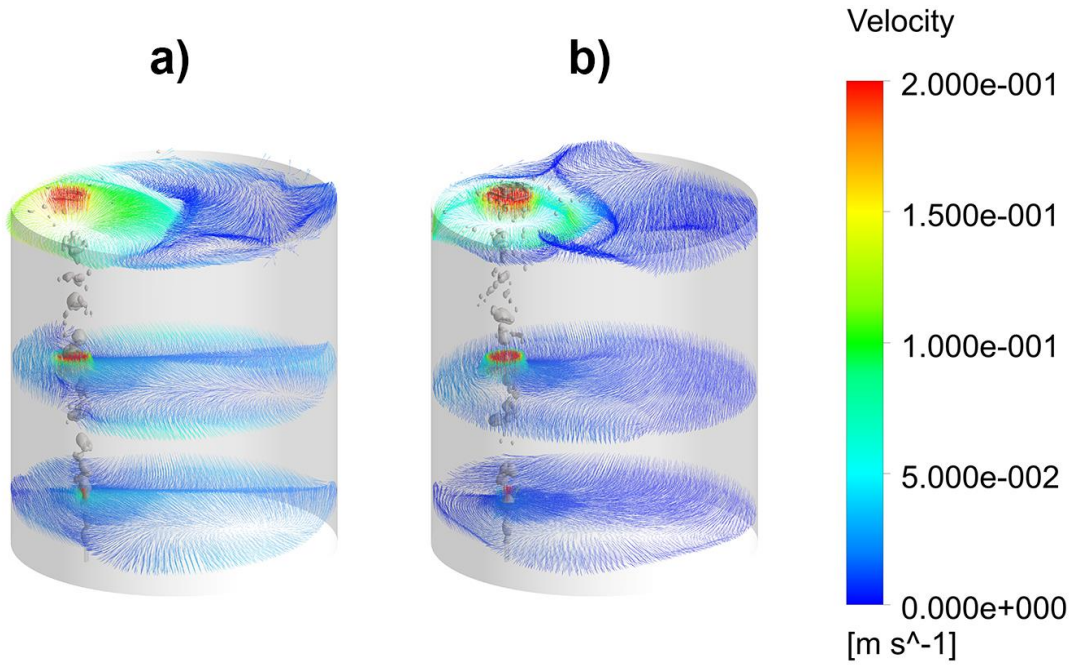

Figure 10. Simulated velocity fields of the liquid phase in different horizontal planes, at 100 mm, 450 mm and 880 mm, for a gas flow rate of $2.14 \times 10^{-4}\ \frac{m^3}{s}$ and different thicknesses of the oil layer. a) 0.02 m. b) 0.04 m.

The proximities of the metal-slag interface are the most important to capture inclusions by the slag phase. Therefore, it is important to understand the turbulence conditions in this region. **Figures 11a-11d** show the measured horizontal-velocities with the ultrasound probe along the distance from the opposite wall of the plume to the wall behind the plume. The dotted line corresponds to the average velocities of the experimental measurements and the interrupted lines correspond to the predictions

Preprints (www.preprints.org) | NOT PEER-REVIEWED | Posted: 17 December 2018 doi:10.20944/preprints201812.0204.v1

of the mathematical model. When there is not an upper layer, **Figure 11a**, the velocity fluctuations near the wall are large and their amplitudes grow at a maximum at the location of the plume due to the bursting effect of the bubbles. Even under the presence of a thin layer, **Figure 11b**, the velocity fluctuations are considerably damped and remain large in the region of the plume by the reason adduced above. As the layer gets thicker, **Figures 11c** and **11d**, the velocity fluctuations suffer further dampening until a condition where practically there are not anymore, those velocity spikes, remaining only those corresponding to the plume. Regarding the mathematical model, although its predictions do not match as well the averaged experimental velocities, they lay inside the magnitudes of the fluctuating velocities. The reasons of this mismatch are basically three, the first is that the VOF model solves only one set of equations for all three phases, the second is that this model predicts averaged velocities of turbulent flows. The third reason is the impossibility to match the computing time with the experimental ones. All these factors impede a good matching between simulations and measurements. However, given these upheavals the mathematical model makes good predictions of the velocities as well.

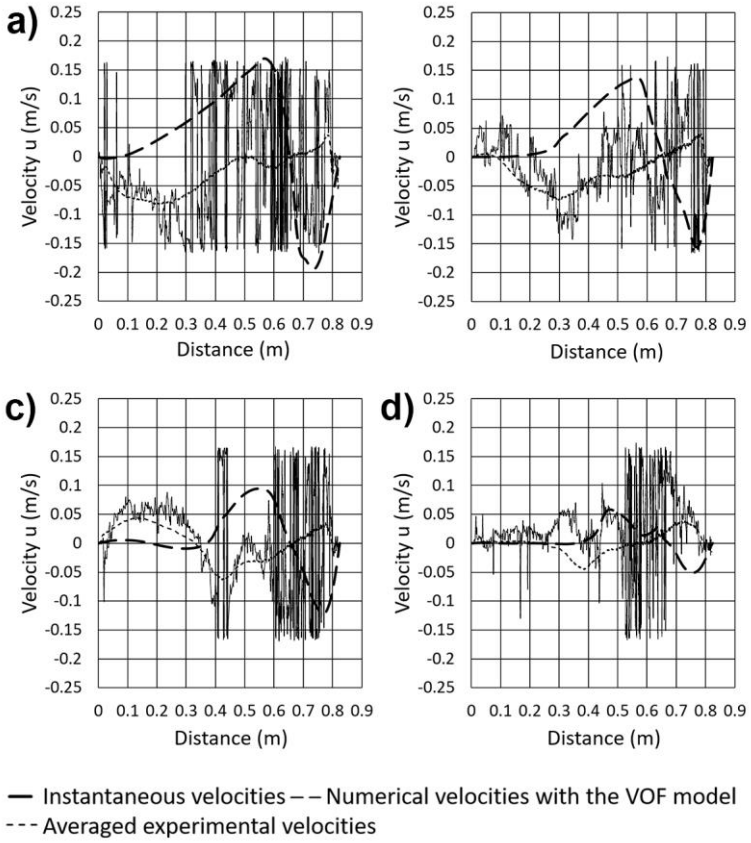

Figure 11. Measured vs simulated velocities 20 mm below the metal-slag interface for different thicknesses of the upper phase layer at a fixed gas flow rate of $1.07 \times 10^{-4}\ m^3/s$. a) 0 m. b) 0.01 m. c) 0.02 m. d) 0.04 m.

Further information about the flow structure in proximities of the metal-slag interface can be seen through the fields of streamlines shown in **Figures 12a-12d** corresponding to **Figures 11a-11d**, respectively. With no upper layer, the stream lines, initiating from the spout follow a regular irradiating pattern. With a thin layer this pattern is slightly disrupted, and two regular vortexes are formed symmetrically in close to the opposite ladle wall. Thicker layers subdivide the flow in many local vortexes with different orientations making the flow practically stagnant.

Preprints (www.preprints.org) | NOT PEER-REVIEWED | Posted: 17 December 2018 doi:10.20944/preprints201812.0204.v1

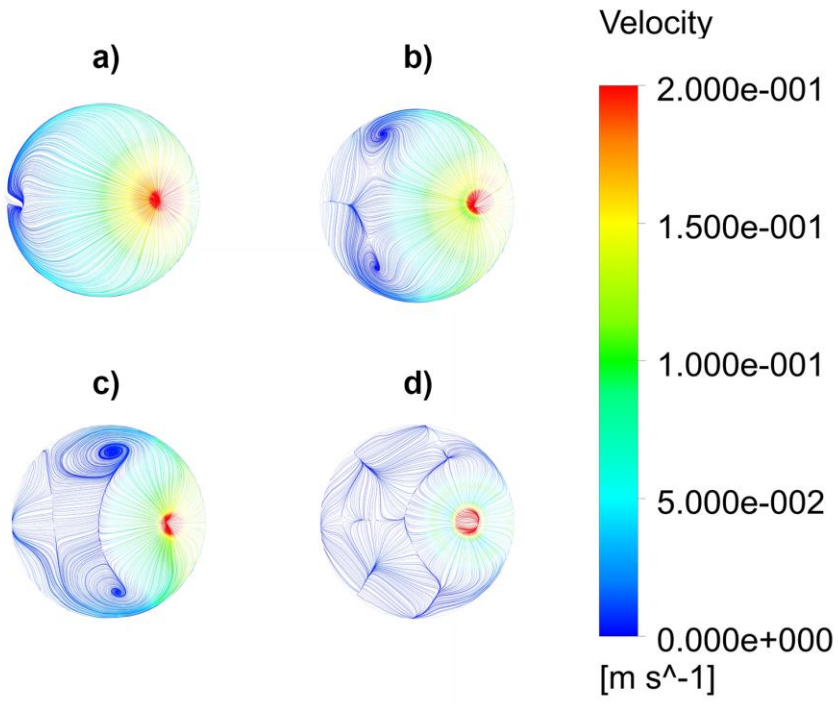

Figure 12. Streamlines of the flow for different thicknesses of the upper layer for a gas flow rate of $2.14X10^{-4}$ m^3/s. a) 0 m. b) 0.01 m. c) 0.02 m. d) 0.04 m.

4.3 Closure

Mixing times are dependent on stirring energy and bath geometry in two-phase flows. In three phase flows mixing time depends on these factors and on the thickness of the slag phase, the physical properties of the upper layer play a secondary role. The SEO area in three-phase flows depends on the flow rate of the stirring gas, the physical properties of the upper layer and on the bath height. As the thickness of the upper layer increases the mixing time increases and the bath approaches to near-stagnant condition. The SEO area increases with the flow rate of gas and decreases with the slag thickness. Denser upper layers favor larger SEO areas and high viscosity layers decrease it.

There have been researches claiming that bubbles play an important role to float out inclusions through mechanism of their adherence on their surfaces [34] and carrying them to the bath surface. Rather, it is the motion of steel, originated by the energy provided by the buoyant bubbles, that carries the inclusions in contact with the slag which, eventually, absorbs them. Hence, it is difficult to agree with this view as their area volume ratio is very small as can be seen in **Figures 9 and 10**. It can be criticized that these simulations do not reflect actual sizes in liquid steel. However, water models always report big bubbles sizes, that may or may not be disintegrated, and given the surface tension of liquid steel, argon bubbles in steel should be twice as large as those observed in the models. Instead is the flow near the proximities of the metal slag-interface which controls the floatation of inclusions. When this region is disrupted by strong forced convection flows the efficiency of floatation decreases. It is only when this region comes to some velocity fields of small magnitude that the efficiency to float inclusions gets high. This explains the need of having what it is called as “rinsing time” which is the last period after refining when the stirring energy is decreased to allow floatation of inclusions in the Stokes regime. This operation is well known by all steelmakers and it is certainly a very necessary one to attain the best of steel cleanliness.

ACKNOWLEDGEMENTS

We give the thanks to IPN and (CoNaCyT) for the support of this work. One of us (RM) gives the thanks to University of Toronto for making possible his stay in Toronto.

Preprints (www.preprints.org) | NOT PEER-REVIEWED | Posted: 17 December 2018 doi:10.20944/preprints201812.0204.v1

REFRENCES

1. K. Krishnapisharhody, G.A. Irons, A Model for Slag Eyes in Steel Refining Ladles Covered with Thick Slag Metall. and Mater. Trans. B, **46B** (2015), 191-198.
2. K. Krishnapisharhody, G.A. Irons, Modeling of Slag Eye Formation over a Metal Bath Due to Gas Bubbling Metall. and Mater. Trans. B, **37B** (2006), 763-772.
3. K. Krishnapisharhody, G.A. Irons, A Study of Spouts on Bath Surfaces from Gas Bubbling: Part II. Elucidation of Plume Dynamics Metall. and Mater. Trans. B, **38B** (2007), 377-388.
4. K. Krishnapisharhody, G.A. Irons, A Study of Spouts on Bath Surfaces from Gas Bubbling: Part I. Experimental Investigation, Metall. and Mater. Trans. **38B**, 2007), 367-375.
5. K. Krishnapisharhody, G.A. Irons, A Unified Approach to the Fluid Dynamics of Gas–Liquid Plumes in Ladle Metallurgy ISIJ. Int., **50** (2010), 1413-1421.
6. M. Iguchi, K. Nakamura, R. Tsujino, Mixing Time and Fluid Flow Phenomena in Liquids of Varying Kinematic Viscosities Agitated by Bottom Gas Injection, Metall. and Mater. Trans. B, **29B** (1998), 569.
7. Dipak Mazumdar, R.I.L. Guthrie, Discussion of "mixing time and fluid flow phenomena in liquids of varying kinematic viscosities agitated by bottom gas injection", Metall. Trans. and Mater. Trans, B, **30B** (1999), 349-351.
8. Dipak Mazumdar, R.I.L. Guthrie, Mixing models for gas stirred metallurgical reactors, Metall. Trans. and Mater. Trans, B Metall. Trans. and Mater. Trans, B, **16B** (1985), 83-90.
9. Dipak Mazumdar, R.I.L. Guthrie, Mixing models for gas stirred metallurgical reactors, Metall. Trans. and Mater. Trans, B, **17B** (1986), 725-733.
10. O. Haida, T. Emi, S. Yamada, F. Sudo, Scaninjet II, Part I, 2nd Int Conf. on Injection Metallurgy, MEFOS-Jerkentoret, 1980, paper 20, Lulea Sweden.
11. Q. Ying, L. Yun, L. Liu, Scaninjet III, Part I, 2nd Int. Conference on Injection Metallurgy, MEFOS-Jernkontoret, 1983, paper 21, Lulea Sweden.
12. B. Li, H. Yin, C.Q. Zhou, F. Tsuikihashi, Modeling of Three-phase Flows and Behavior of Slag/Steel Interface in an Argon Gas Stirred Ladle, ISIJ Int., **48** (2008), 1704-1711.
13. Z. Liu, L. Li, B. Li, ISIJ International, Modeling of Gas-Steel-Slag Three-Phase Flow in Ladle Metallurgy: Part I. Physical Modeling, **57** (2017), 1971.
14. U. Singh, R. Anapagaddi, S, Mangal, K. A. Padmanabhan and A.K. Singh, Metall. and Matter. Trans. B, Multiphase Modeling of Bottom-Stirred Ladle for Prediction of Slag–Steel Interface and Estimation of Desulfurization Behavior, **47B** (2016), 1804-1816.
15. D. Mazumdar, R.I.L. Guthrie, Modeling Energy Dissipation in Slag-Covered Steel Baths in Steelmaking Ladles Metall. and Mater. Trans. B, **41B** (2010), 976-989.
16. L.T. Khajavi, M. Barati, Metall. and Mater. Trans. B, Liquid Mixing in Thick-Slag-Covered Metallurgical Baths—Blending of Bath, **41B** (2010), 86-93.
17. P.G. Jonsson L. Jonsson, D. Sichen, ISIJ Int., Viscosities of LF Slags and Their Impact on Ladle Refining, **37** (1997), 484-491.
18. S. Yamashita, K. Miyamoto, M. Iguchi, M. Zeze, Model Experiments on the Mixing Time in a Bottom Blown Bath Covered with Top Slag, ISIJ Int., **43** (2003), 1858-1860.
19. D. Mazumdar, D.S. Kumar, Proc. Oxygen Steelmaking Conf. G Irons and S. Sun Eds., Met, Soc. CIM Hamilton Canada, 2004, 311.
20. S. Patil, D. Satish, M. Paranandhanatham, D. Mazumdar, Mixing Models for Slag Covered, Argon Stirred Ladles, ISIJ Int., **50** (2010). 1117-1124.
21. A.M. Amaro-Villeda, M.A. Ramirez-Argaez, A.N. Conejo, Effect of Slag Properties on Mixing Phenomena in Gas-stirred Ladles by Physical Modeling ISIJ Int., **54** (2014), 1-8.
22. K. Yonezawa , K. Scherdtfeger, Spout eyes formed by an emerging gas plume at the surface of a slag-covered metal melt, *Metall. Trans.*, **30B** (1999), 411-418.
23. Subagyo, G.A. Brooks, G.A. Irons, Spout Eyes Area Correlation in Ladle Metallurgy, ISIJ Int., **43 (**2003), 262-263.
24. K. Krishnapisharhody, G. A. Irons, An Extended Model for Slag Eye Size in Ladle Metallurgy, ISIJ Int., Vol. **48** (2008), No. 12, pp. 1807-1809.
25. M. Peranandhanthan, D. Mazumdar, Modeling of Slag Eye Area in Argon Stirred Ladles, ISIJ Int., **50** (2010), 1622-1631.
26. http://imagej.nih.gov/ij/index.html. ImageJ-1.49 (Image Processing and Analysis in Java). Consulted in October 2018.
27. C.W. Hirth, B.D. Nichols, Volume of fluid (VOF) method for the dynamics of free boundaries, *J. of Comp. Phys*., **39**, (1981), 201-225.
28. H. Ferziger, M. Peric, *Computational Methods for Fluid Dynamics*, (Berlin, New York, Springer 2002), 72-75.
29. J.U. Brackbill, D.B. Kothe, C. Zemack, A continuum method for modeling surface tension, J. *Comp. Phys*., **100**, (1992), 335-354.

Preprints (www.preprints.org) | NOT PEER-REVIEWED | Posted: 17 December 2018 doi:10.20944/preprints201812.0204.v1

30. S.B. Pope: “Turbulent Flows”, Cambridge Press, New York N.Y. Cambridge, London, (2000), 387-457.
31. D.C. Wilcox, “Turbulence Modeling for CFD”, D.C.W. Industries Inc, La Cañada CA, (2000), 103-218.
32. www. ansys.com
33. Z. Han, L. Holappa, Mechanisms of Iron Entrainment into Slag due to Rising Gas Bubbles, ISIJ Int., 43 (2003, 292-297.
34. M. Soder, P. Jonsson, L. Jonsson, Inclusion Growth and Removal in Gas-Stirred Ladles, Steel Research International, 75 (2004), 128-138.
35. S.N. Sahasrabudhe, V. Rodriguez-Martinez, M. O’Meara, B, E. Farkas Int. J. of Food Properties, **20** (2017), S1965-S1981.